

A theory for the response of tropical moist convection to mechanical orographic forcing

QUENTIN NICOLAS*

Department of Earth and Planetary Science, University of California, Berkeley, California

WILLIAM R. BOOS

*Department of Earth and Planetary Science, University of California, Berkeley, California
Climate and Ecosystem Sciences Division, Lawrence Berkeley National Laboratory, Berkeley, California*

ABSTRACT

Spatial patterns of tropical rainfall are strongly influenced by mountains. Although theories for precipitation induced by convectively stable upslope ascent exist for the midlatitudes, these do not represent the interaction of moist convection with orographic forcing. Here, we present a theory for convective precipitation produced by the mechanical interaction of a tropical ridge with a basic state horizontal wind. Deviations from this basic state are represented as the sum of a ‘dry’ perturbation, due to the stationary orographic gravity wave, and a ‘moist’ perturbation that carries the convective response. The moist component dynamics are vertically truncated and subject to the weak temperature gradient approximation; they are forced by the dry mode’s influence on lower-tropospheric moisture and temperature. Analytical solutions provide estimates of the precipitation profile, including peak precipitation, upstream extent, and rain shadow extent. The theory can be used with several degrees of complexity depending on the technique used to compute the dry mode, which can be drawn from linear mountain wave theory or full numerical simulations. To evaluate the theory, we use a set of convection-permitting simulations with a flow-perpendicular ridge in a long channel. The theory makes a good prediction for the cross-slope precipitation profile, indicating that the organization of convective rain by orography can be quantitatively understood by considering the effect of stationary orographic gravity waves on a lower-tropospheric convective quasiequilibrium state.

1. Introduction

The spatial distribution of time-mean low-latitude rainfall is set to first order by the latitude and intensity of the intertropical convergence zone (ITCZ). Zonal inhomogeneities in sea-surface temperatures, a direct consequence of the presence of land masses, modify this distribution by driving the Walker circulation. These land masses also act seasonally as strong energy sources that drive monsoon circulations. On sufficiently large length scales, one might be satisfied with this description of the principal features and forcings of tropical precipitation; looking in more detail, however, one sees that orography strongly modifies these broad patterns.

Satellite-derived estimates (TRMM 3B42, Huffman et al. 2007) of climatological precipitation for June–August and October–December are shown in Figure 1a,b, along with a smoothed contour of 500 m surface height. Some of the most striking deviations from the quasi-linear oceanic ITCZ are regions of intense rainfall located in the vicinity of mountains, e.g. near the Northern Andes, Western Ghats, Himalayas, and various ranges in the Indochinese peninsula and Maritime continent. These precipitation maxima are located in regions and seasons favorable to moist convective development, as noted by Xie et al. (2006)

for the Asian summer monsoon and Ramesh et al. (2021) for regions experiencing an autumn monsoon. Xie et al. (2006) note that despite their prominence, a regional atmospheric model with a 0.5° resolution is unable to reproduce these features. This failure, partly attributed to inadequate convective parameterization, was confirmed in a more systematic study by Kirshbaum (2020). It suggests that our main tool for evaluating climate, namely global circulation models, is ill-suited to study orographic convection, despite its importance for tropical precipitation.

Kirshbaum et al. (2018) identify two ways orography generates or alters convective systems: mechanical forcing, whereby a mountain lifts a background wind, and thermal forcing, where surface heat fluxes from elevated terrain produce convergence. Figure 1 displays 100 m wind vectors from the ERA5 reanalysis (Hersbach et al. 2020). Enhanced precipitation is mostly focused upwind of mountain ranges, suggesting that mechanical forcing is the primary mechanism at play in the large-scale, climatological sense. To further illustrate this point, we plot cross-sections of surface elevation and precipitation for summer and autumn along a latitude line spanning India, Southeast Asia, and the Philippines. We observe a clear shift of rainfall maxima from the western slopes in summer to the eastern slopes in autumn, consistent with the seasonal wind reversal in these regions.

*Corresponding author: Quentin Nicolas, qnicolas@berkeley.edu

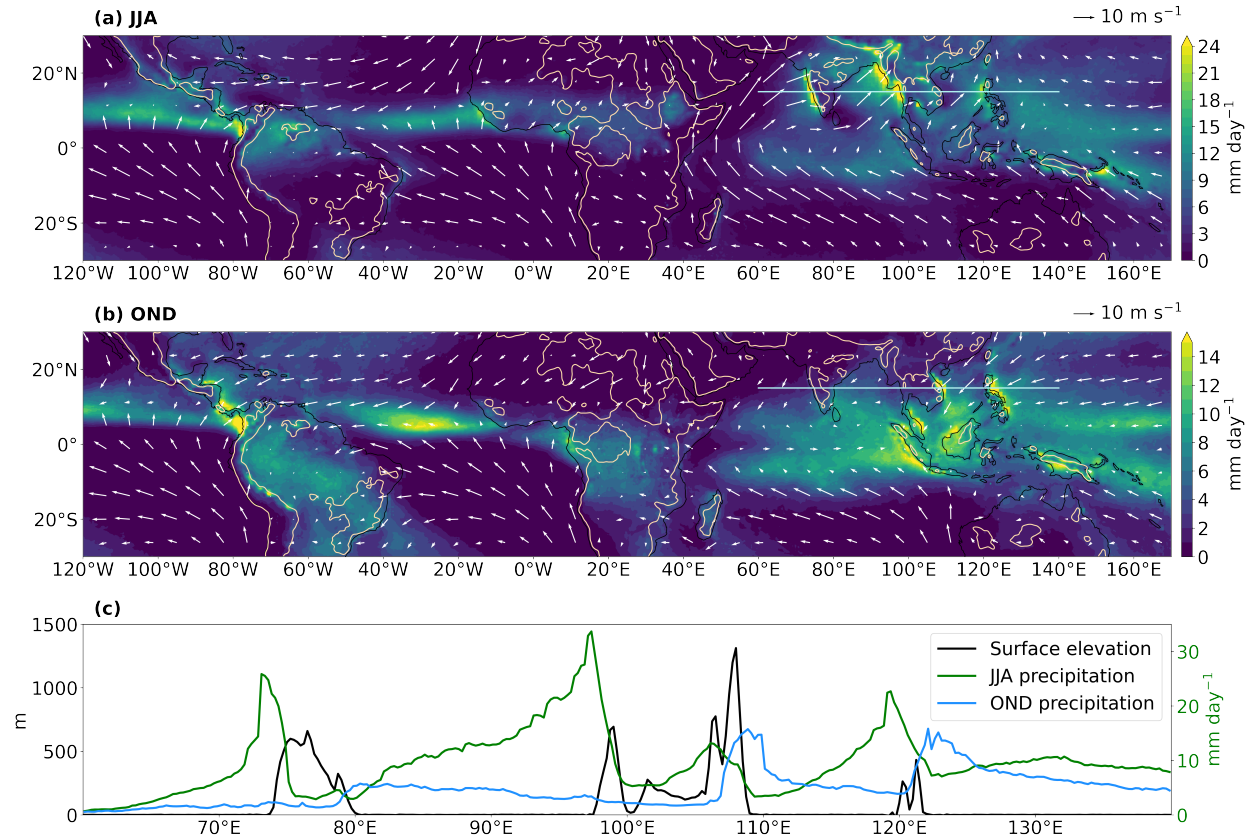


FIG. 1. Annual-mean TRMM 3B42 mean precipitation (shading), 500 m surface height level (thin brown contours), and wind vectors 100 m above the surface averaged over (a) June-August and (b) October-December. (c) Cross-sections of surface elevation and precipitation along the thick blue line shown on panels a and b at 15°N.

Orographic precipitation in midlatitude, convectively stable flows has been extensively studied (for a review, see e.g. Roe 2005)). Smith and Barstad (2004) developed an analytical theory, using linear mountain wave dynamics, that efficiently reproduces rainfall rates and spatial organization in such cases. However, because it does not account for the feedback of moist convection on mountain-induced motion, this theory is not applicable to most tropical cases.

Orographic convection has been the focus of field experiments and numerous studies in the past two decades (Houze 2012; Kirshbaum et al. 2018). However, most have focused on synoptic scales, with little attention devoted to understanding what sets climatological time-mean precipitation rates. Chu and Lin (2000) and Chen and Lin (2005) studied initial value problems, where the fate of conditionally unstable flow was qualitatively examined as a function of moist nondimensional mountain height and convective available potential energy (CAPE). Miglietta and Rotunno (2009) extended their work to study the dependence on a more exhaustive set of parameters, noting that precipitation increased both with the ratio of mountain height to the level of free convection, and with the aspect ratio of the moun-

tain. The ratio of advective to convective time scales was shown to control the shape of the cross-mountain rainfall profile, with wider mountains having their precipitation profile shifted upstream. Subsequent studies (Miglietta and Rotunno 2012, 2014) noted the importance of vertical wind shear in producing large rain rates in the presence of deep convection; soundings with strong flow at lower levels and weak flow aloft produced higher precipitation rates. Focusing on larger spatial and temporal scales, Wang and Sobel (2017) simulated rainfall over isolated tropical islands in both thermally and mechanically forced settings. Their flat-island cases showed that surface roughness gradients alone can produce substantial mechanical forcing for precipitation, and that the transition from thermal to mechanical forcing can cause a non-monotonic dependence of mean precipitation on upstream wind speed.

Few studies attempted to formulate theories for orographically forced moist convection. Kirshbaum and Smith (2009) took inspiration from trade-wind flows over Dominica to develop an analytical model for the orographic enhancement of precipitation from shallow convection. They used a ‘slice’ method separating saturated updrafts

from unsaturated descending air, computing the impact of an imposed mean ascent on vertical velocities. Two elements hamper application of this theory to the time-mean effects of orography on deep convection. First, the mean ascent is assumed to be uniform in height, whereas deep convection spans at least one vertical wavelength of an orographic gravity wave. Second, the theory contains multiple unconstrained parameters (e.g., updraft area fraction, an ‘entrainment’ parameter representing dissipative effects on cloudy updrafts) that would vary greatly on time scales larger than those of a single event. To the best of our knowledge, Cannon et al. (2014) is the only analytical work focused on orographic deep convection, having developed an area-averaged model with detailed microphysics. The precipitation rate is computed level-wise by bringing parcels to their level of neutral buoyancy, then accounting for detrainment and evaporation due to compensating descent before applying a CAPE-dependent weighting. The model leads to a high number of equations to be solved, hindering physical insights, and its “bulk” nature obscures key questions such as how far upstream precipitation is enhanced and how long the rain shadow is.

A fruitful line of development in the theory of tropical dynamics has been the quasiequilibrium (QE) view of convection, dating back to Arakawa and Schubert (1974) and outlined by Emanuel et al. (1994). This view has its roots in the observation that CAPE varies slowly compared to its large-scale generation mechanisms, and is consumed by convective motions on comparatively short time scales. Convective motions are thus in near statistical equilibrium with the large scales, in that they set the vertical temperature profile, tying it directly to the subcloud-layer moist static energy. The relevance of QE theory to orographically forced convection is suggested by the observation of Roe (2005) and Houze (2012) that orography often modifies pre-existing precipitating systems rather than triggering new convection. Describing the statistical average effect of mountains on convection, rather than formulating a theory of convective triggering, may be more faithful to this observational reality. While early QE theories employed CAPE-based convective closures, recent developments incorporate observed relationships between precipitation and lower-tropospheric temperature and humidity (Derbyshire et al. 2004; Raymond et al. 2015; Ahmed et al. 2020).

This work builds upon QE thinking to propose a theory for the interaction of moist convective precipitation with orographic mechanical forcing. We pose two key questions: what sets the mean precipitation rate of mechanically-forced orographic convection? How far upstream and downstream does orography influence tropical precipitation? Unlike some classic QE closures that only consider near-surface temperature and moisture anomalies, we use a convective closure that is sensitive to lower free tropospheric anomalies, and accounts for the influence of stationary orographic gravity waves on those anomalies.

This links classic stationary wave theory with modern QE closures for convection, and provides nonlinear expressions for precipitation as well as a linearized theory that can be forced by the Fourier transformed terrain. Convection-permitting simulations in a long channel are used to test theoretical rain rates. We use the results of these simulations to evaluate the convective time scales used in the theory and the possible influence of spatial modulations of surface evaporation and radiative cooling downwind of the ridge.

2. Theory

This section presents an analytical theory for the precipitation around a tropical mountain in a background wind, based on a QE convective closure. Its aim is to account for the main features of time-mean precipitation around the ridge (peak value, spatial extent of upstream enhancement, rain shadow length), as a function of large-scale flow characteristics and ridge shape. The theory is based loosely on the Quasiequilibrium Tropical Circulation Model (QTCM) of Neelin and Zeng (2000), but employs the moisture-temperature ($q - T$) convective parameterization proposed by Ahmed et al. (2020). This closure was derived from the empirical relationship between precipitation and lower-free-tropospheric buoyancy and parameterizes precipitation as a response to both temperature and moisture perturbations, with different sensitivities. The reason we chose to use this closure instead of a more classic CAPE-based parameterization will be expanded upon in section 3b. Our main hypothesis, assessed in later sections, is that mountains alter convection by modulating lower-tropospheric temperature and moisture. In the presence of a background wind, an orographic gravity wave is excited that carries thermodynamic perturbations. Forced ascent upwind of the ridge cools and moistens the lower troposphere, enhancing convection. The opposite occurs downstream where subsidence prevails. In addition to these orographically induced thermodynamic variations, we will show that the solution depends on a characteristic length for relaxation to radiative-convective equilibrium (RCE), and on the convective adjustment time scales.

a. Modal decomposition

Throughout this paper, we consider a horizontally infinite low-latitude domain with surface elevation $h(x)$ and a uniform and constant background horizontal wind \mathbf{u}_0 . As explained in appendix A, linearizing the dynamics allows the flow to be described as the sum of a basic state and two perturbation modes: a dry mode, due solely to the orographic gravity wave, and a moist mode, that represents the moist convective part of the flow. The dry mode only influences the moist mode as a forcing for convective heating, while the moist mode does not influence the dry mode. Steady-state thermodynamic and moisture

equations for the moist mode are

$$\mathbf{u}_0 \cdot \nabla T_m + \omega_m \frac{\partial s_0}{\partial p} = Q_c - R, \quad (1a)$$

$$\mathbf{u}_0 \cdot \nabla q_m + \omega_m \frac{\partial q_0}{\partial p} = Q_q + E, \quad (1b)$$

where $s_0(p)$ and $q_0(p)$ are, respectively, the dry static energy and moisture vertical profiles, with the zero subscript denoting a property of the basic state, and ω_m , T_m , and q_m are the pressure velocity, temperature, and moisture perturbations of the moist mode. Q_c and Q_q denote convective heating and moistening, while R and E are radiative cooling and evaporation rates. Here, and subsequently, temperature and moisture are in energy units (i.e. they have, respectively, absorbed the heat capacity of air at constant pressure c_p , and the latent heat of vaporization of water L_v).

We now perform a QTGM-like unimodal vertical truncation of the moist mode. We only include a deep convective mode, with any shallow temperature anomaly induced by the orographic gravity wave represented by the dry mode. This treatment likely renders our theory most appropriate for tropical regions. Following Sobel et al. (2001), we also employ the weak temperature gradient (WTG) approximation for the moist mode, which allows us to solve for that mode without the momentum equations (remember that horizontal temperature gradients induced by the orographic gravity wave are carried by the dry mode). Using notation from Neelin and Zeng (2000), we write $\omega_m(x, y, p) = \omega_1(x, y)\Omega_1(p)$, and we use M_s , M_q and $M = M_s - M_q$ to denote the gross dry stability, gross moisture stratification, and gross moist stability (GMS), respectively. Vertically averaging (1a)-(1b) and eliminating ω_1 yields

$$\mathbf{u}_0 \cdot \nabla \langle q_m \rangle - \langle Q_q \rangle - \langle E \rangle - \frac{M_q}{M_s} (\langle Q_c \rangle - \langle R \rangle) = 0, \quad (2)$$

where $\langle \cdot \rangle$ denotes a tropospheric average in pressure coordinates. We now introduce the energy constraint $\langle Q_c \rangle = -\langle Q_q \rangle$ and employ the $q-T$ convective closure,

$$\langle Q_c \rangle = \left(\frac{q'_L}{\tau_q} - \frac{T'_L}{\tau_T} \right)_+, \quad (3)$$

where $(\cdot)_+ = \max(\cdot, 0)$. τ_q and τ_T are the moisture and temperature adjustment time scales, diagnosed respectively as approximately 11 hours and 3 hours by Ahmed et al. (2020). q'_L and T'_L are deviations from the reference profiles of moisture and temperature, with the subscript L denoting a lower-free-tropospheric average. Decomposing these anomalies into contributions from the moist and dry modes (subscripts m and d , respectively, see also Appendix A) gives

$$q'_L = q_{mL} + q_{dL} \text{ and } T'_L = T_{mL} + T_{dL} = T_{dL}, \quad (4)$$

where the last equality comes from WTG (if temperature gradients are zero, one can choose $T_m = 0$ by simply shifting T_0). The heating term (3) will have two contributions: one from the dry perturbations q_{dL} and T_{dL} (hereafter referred to as “the dry forcing for convection”), and a moist convective response carried by q_{mL} . Because we assumed a horizontally and temporally invariant vertical profile for q_m , the quantities q_{mL} and $\langle q_m \rangle$ are proportional. Using the notation of Ahmed et al. (2020), $q_{mL}/\tau_q = \langle q_m \rangle/\tilde{\tau}_q$, where $\tilde{\tau}_q \simeq 0.6\tau_q$.

b. Nonlinear theory

We can now obtain an equation for precipitation. Define $p_T = p_s - p_t$, the tropospheric depth, where p_s and p_t are respectively surface and tropopause pressures. We set the tropospheric mass per unit area as $p_T/g = 8000 \text{ kg m}^{-2}$ henceforth. Precipitation is given by $P = p_T \langle Q_c \rangle / g$ in units of energy per unit area per unit time (dividing by $\rho_w L_v$, where ρ_w is the density of liquid water, yields a physical precipitation rate, in m s^{-1}). One can use this with (2), (3), and (4) to obtain an equation for P :

$$\mathbf{u}_0 \cdot \nabla P = \left[-\frac{M}{M_s \tilde{\tau}_q} (P - P_0) + \frac{p_T}{g} \mathbf{u}_0 \cdot \nabla \left(\frac{q_{dL}}{\tau_q} - \frac{T_{dL}}{\tau_T} \right) \right] \mathcal{H}(P),$$

where $P_0 = \frac{p_T}{g} \frac{M_s \langle E \rangle - M_q \langle R \rangle}{M} \quad (5)$

and \mathcal{H} denotes the Heaviside function. We henceforth drop the y dependence, simplifying (5) to

$$\frac{dP}{dx} = \left[-\frac{P - P_0}{L_q} + \frac{p_T}{g} \frac{d}{dx} \left(\frac{q_{dL}}{\tau_q} - \frac{T_{dL}}{\tau_T} \right) \right] \mathcal{H}(P), \quad (6)$$

where $L_q = u_0 \tilde{\tau}_q \frac{M_s}{M}$.

Note that in a state of RCE, $\langle E \rangle = \langle R \rangle$, hence the basic state precipitation $P_0 = p_T \langle E \rangle / g$, which is the column-integrated evaporation rate. (6) is essentially a forced equation with P relaxed towards P_0 on the length scale L_q . Hence, if the dry forcing $\langle q_d \rangle / \tau_q - \langle T_d \rangle / \tau_T$ is felt on a distance significantly shorter than L_q , the latter will dominate in setting the length of the downstream rain shadow.

L_q can be understood as a Lagrangian convective length scale, whereby a column traveling at velocity u_0 undergoes moisture adjustment on a time scale $\tilde{\tau}_q$. It is also inversely proportional to the relative GMS M/M_s , which measures the efficiency with which a column exports energy and thus returns to an equilibrium state. L_q is vanishingly small, and the dry forcing is felt on equally small distances, in the limit of zero wind (no advection), instantaneous convective adjustment, or infinite GMS (allowing for instantaneous return to equilibrium). We estimate a ratio $M/M_s = 5$ (see section 4b) so that for $u_0 = 10 \text{ m s}^{-1}$, $L_q \simeq 1000 \text{ km}$, which indicates that the mountain’s effect is felt over a large downstream distance. Such an extensive rain shadow may seem

unrealistic, but in real cases large-scale processes and flow detouring around topography can shorten the rain shadow. A time-varying cross-slope wind, including episodes of reversed flow, would further shorten the time-mean rain shadow. Note however that Biasutti et al. (2012) documented a very broad rain shadow downwind of Sri Lanka during the Indian summer monsoon.

c. Linear theory

Equation (6) can be solved for the precipitation field as a function of moisture and temperature perturbations induced by “dry” mountain flow. These perturbations can in turn be obtained with several degrees of complexity, from a full mountain wave simulation to a linear solution with uniform background stratification. Here, in the spirit of the linear model of Smith and Barstad (2004), we employ linear mountain wave theory to obtain a closed expression relating mountain shape to precipitation in the Fourier domain.

The linearized thermodynamic and moisture equations of the dry mode (see Appendix A) read

$$u_0 \frac{dT_d}{dx} + w_d \frac{ds_0}{dz} = 0, \quad u_0 \frac{dq_d}{dx} + w_d \frac{dq_0}{dz} = 0, \quad (7)$$

where we used height coordinates and dropped the y dependence. Hence, the dry forcing for convection in (6) becomes

$$\frac{d}{dx} \left(\frac{q_{dL}}{\tau_q} - \frac{T_{dL}}{\tau_T} \right) = \frac{w_d L}{u_0} \left(\frac{1}{\tau_T} \frac{ds_0}{dz} - \frac{1}{\tau_q} \frac{dq_0}{dz} \right). \quad (8)$$

We assume that ds_0/dz and dq_0/dz do not depend on z and define the constant χ as the sum of two terms both contributing to enhanced convection,

$$\chi = \frac{p_T}{g} \left(\frac{1}{\tau_T} \frac{ds_0}{dz} - \frac{1}{\tau_q} \frac{dq_0}{dz} \right). \quad (9)$$

These two terms represent, respectively, lower tropospheric cooling (due to adiabatic ascent), and moistening (also due to ascent along a vertically decreasing moisture profile, $dq_0/dz < 0$). To obtain a linear equation, the nonlinear Heaviside function in (6) has to be dropped; this amounts to allowing negative Q_c , which only influences the solution in the downstream region, where drying and warming by the dry mode predominate. We now substitute (8) and (9) into the linearized (6) and take the Fourier transform, yielding

$$ik \hat{P}'(k) + \frac{\hat{P}'(k)}{L_q} = \frac{\hat{w}_{dL}(k)}{u_0} \chi, \quad (10)$$

where $P' = P - P_0$, k is the horizontal wavenumber and the Fourier transform is denoted with a hat. Linear, Boussinesq

mountain wave theory expresses \hat{w}_d as (e.g., Smith 1979)

$$\hat{w}_d(k, z) = ik u_0 \hat{h}(k) e^{im(k)z}$$

$$\text{and } m(k) = \begin{cases} \sqrt{l^2 - k^2} & \text{if } k^2 < l^2 \\ i\sqrt{k^2 - l^2} & \text{if } k^2 > l^2 \end{cases}, \quad (11)$$

where $l = N/u_0$ and N is the Brunt-Väisälä frequency, assumed positive and constant with height. N is related to the basic state lapse rate by $N^2 \simeq (g/C_p T_0) ds_0/dz$, with T_0 a reference temperature taken as 300 K. We have also assumed that the density of air is uniform, given that perturbations are averaged over the lower troposphere only. Combining (10) and (11) gives the final relationship:

$$\hat{P}'(k) = \frac{ik\chi}{ik + 1/L_q} \hat{h}(k) \left(e^{im(k)z} \right)_L. \quad (12)$$

After solving for P' , negative values of precipitation are avoided by applying the $(\cdot)_+$ operator to $P' + P_0$. The above linear expression for convective orographic precipitation is meant to represent time-mean rain rates, as opposed to single-event or extreme precipitation. It depends on two parameters (τ_q and τ_T) and a number of physical quantities: u_0 , N , the moisture lapse rate dq_0/dz , the mountain profile $h(x)$, and, through L_q , the relative GMS M/M_s . We now explore sample solutions with idealized mountain profiles to illustrate predictions of this theory.

d. Example profiles

To illustrate the behavior of (12), we choose the classic Witch-of-Agnesi profile $h(x) = h_0 l_0^2 / (x^2 + l_0^2)$, where l_0 is the mountain half-width and h_0 is the maximum height. We use $\tau_T = 3$ hours, $\tau_q = 11$ hours, and $M_s/M = 5$. The basic state wind u_0 is set to 10 m s^{-1} , which yields $L_q = 1188 \text{ km}$. We set $N = 0.01 \text{ s}^{-1}$, or equivalently $ds_0/dz \simeq 3 \text{ J kg}^{-1} \text{ m}^{-1}$ or 3 K km^{-1} . The lower tropospheric average in (12) is taken between $z = 1000 \text{ m}$ and 3000 m . The moisture lapse rate is computed as an average over the same layer of the profile $q_0(z) = r q_{\text{sat}}(T_s) e^{-z/H_m}$ where $r = 0.8$, $T_s = 300 \text{ K}$ and $H_m = 2500 \text{ m}$, which yields $dq_0/dz \simeq 8.1 \text{ J kg}^{-1} \text{ m}^{-1}$. Finally, the equilibrium precipitation $P_0 = 4 \text{ mm day}^{-1}$.

Using a fast Fourier transform (FFT), we compute solutions with two different mountain heights and varying τ_T and τ_q (Fig. 2). The reference case uses the time scales computed by Ahmed et al. (2020) and $h_0 = 1000 \text{ m}$. Precipitation is significantly enhanced starting 1500 km upstream and peaks near the steepest slope of the ridge’s windward side, with a 7-fold enhancement compared to the undisturbed P_0 . Downwind, the rain shadow is about 1000 km long and precipitation overshoots P_0 before slowly relaxing back towards it. This behavior can be understood as follows: immediately downwind of the mountain, the dry perturbation is warm and dry in the lower troposphere, hence $\langle q_m \rangle$ increases (on a length scale given by L_q) as

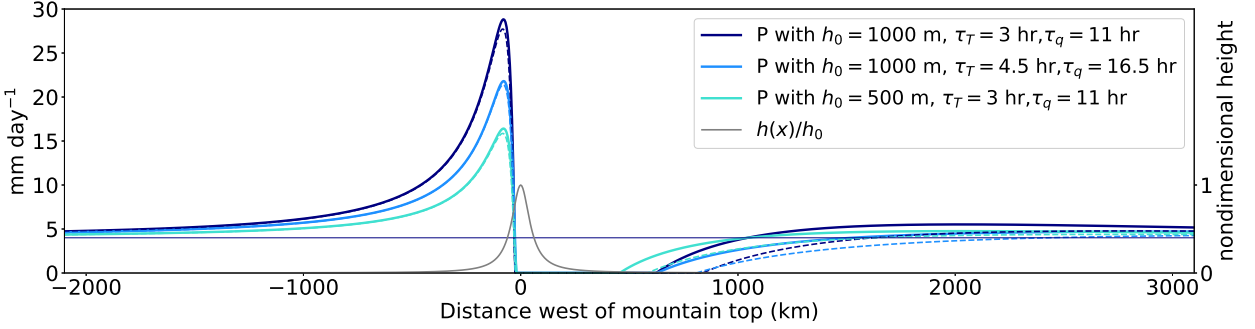


FIG. 2. Precipitation predicted by the linear theory (12) with a Witch-of-Agnesi mountain profile and varying mountain heights and adjustment time scales (solid lines). Dashed lines show the approximate analytical expression (15). The thin horizontal line shows the basic-state precipitation P_0 .

precipitation is suppressed, and precipitation approaches P_0 . Meanwhile, the dry perturbation weakens as it moves away from the ridge (i.e., $q_{dL}/\tau_q - T_{dL}/\tau_T$ becomes less negative), and the positive q_m that accumulated downwind of the mountain leads to the overshoot, $P > P_0$.

A second case shows that increasing the convective time scales by 50% mainly produces a proportional decrease in the upstream precipitation perturbation. This occurs because, in the linear solution (12), P' is proportional to χ , which is in turn inversely proportional to the time scales. The change in L_q , which increases with τ_q , primarily lengthens the rain shadow. The last example confirms that, in this linear framework, halving h_0 , while keeping other parameters constant, exactly halves P' .

Linear flow around a Witch-of-Agnesi ridge admits approximate analytical solutions, allowing us to diagnose the various scales involved. We integrate (10), yielding

$$\begin{aligned} P' &= \chi \int_{-\infty}^x \frac{w_{dL}(x')}{u_0} e^{-\frac{x-x'}{L_q}} dx' \\ &= \chi \zeta_L(x) - \chi \int_{-\infty}^x \frac{\zeta_L(x')}{L_q} e^{-\frac{x-x'}{L_q}} dx' \end{aligned} \quad (13)$$

after integrating by parts and noting that $w_d(x', z) = u_0 \partial \zeta(x', z) / \partial x'$, where $\zeta(x', z)$ is the vertical displacement at x' of a streamline originating upstream at z . Defining $k_s = N/u_0$ and noting that $l_0 k_s \gg 1$ for mesoscale ridges ($1/k_s \approx 1$ km), ζ can be approximated as (Queney 1948)

$$\zeta(x, z) = h_0 \frac{l_0^2 \cos(k_s z) - l_0 x \sin(k_s z)}{x^2 + l_0^2}, \quad (14)$$

where h_0 and l_0 are the Witch-of-Agnesi parameters defined above. We define $c = (\cos(k_s z))_L, s = (\sin(k_s z))_L$. The second term on the right-hand side of (13) acts as a damping over large spatial scales, hence we approximate $\zeta_L \approx -h_0 l_0 s / x$ in that term. We obtain

$$P' \approx \chi h_0 \left[\frac{cl_0^2 - sl_0 x}{x^2 + l_0^2} + \frac{sl_0 e^{-x/L_q}}{L_q} \text{Ei}(x/L_q) \right], \quad (15)$$

where Ei is the exponential integral function. This approximate expression agrees well with the full numerical solution upwind of the mountain (Figure 2, dashed lines).

The location of the precipitation maximum can be diagnosed accurately for cases where $l_0/L_q \ll 1$ by neglecting the last term in (15). One obtains

$$x_{\max} = -l_0 \left(\sqrt{1 + \frac{c^2}{s^2}} - \frac{c}{s} \right). \quad (16)$$

With the above parameters, it lies 76 km upstream, i.e. slightly upstream of the steepest point $x = -l_0$ (note that with this value of k_s , $s > 0$ and $c < 0$). The associated precipitation maximum is

$$P_{\max} = P_0 + \chi h_0 s / [2(\sqrt{1 + c^2/s^2} - c/s)]. \quad (17)$$

The exponential integral term provides a more important correction for P_{\max} than for x_{\max} : (17) overestimates P_{\max} by about 30% for the above cases.

We can also obtain from (15) an order of magnitude for the upstream extent of the precipitation enhancement, defined as the location x_u where P' exceeds a threshold δP . Far from the ridge, neglecting the last term of (15) for tractability, we find $P'(x) = -s \chi h_0 l_0 / x$, hence

$$x_u \sim -l_0 (s \chi h_0 / \delta P). \quad (18)$$

With the above values for χ , s , and l_0 , and for $h_0 = 1000$ m and $\delta P = 1 \text{ mm day}^{-1}$, $x_u = -5000$ km. Thus, x_u has the same order of magnitude as L_q , and the exponential integral term is expected to matter at these scales; indeed, the exact x_u obtained from the full linear solution is around 1700 km, which is a substantial correction. Nevertheless, the general dependence on various parameters is captured.

e. Summary

The theory presented in this section uses a quasiequilibrium closure to solve for the convective precipitation

forced by a dry orographic gravity wave, through its modulation of lower tropospheric temperature and moisture. The most general equation is (5); it retains the nonlinearity of the convective closure and applies to flows with two horizontal dimensions. Dropping a horizontal dimension leads to (6) and introduces L_q , the Lagrangian convective length scale on which precipitation converges to its equilibrium value P_0 ; which is also the rain shadow length scale in cases where the dry forcing is felt on small distances. This nonlinear theory lacks a closure for the dry perturbations induced by the orographic gravity wave.

Treating the orographic gravity wave linearly, and neglecting the nonlinearity of the convective closure, yields equation (12); this is a closed theory relating mountain shape to the spatial profile of convective precipitation, in the spirit of Smith and Barstad (2004). The theory depends on a number of physical quantities and the time scales of the convective closure, τ_T and τ_q . Whilst (12) can be solved numerically with a FFT, approximate analytical expressions are obtained in the case of a Witch-of-Agnesi terrain, yielding expressions for the location of the precipitation maximum and the upstream extent of the precipitation enhancement.

3. Numerical simulations

This section presents the framework we use to test the theory: a set of convection-permitting simulations in which a constant horizontal background flow in a long channel encounters a ridge. In addition to comparing simulated precipitation from this model with our theory, we evaluate the validity of the QE and WTG approximations.

a. Simulation setup

We use a three-dimensional idealized version of the Weather Research and Forecasting model (WRF-ARW, version 4.1.5, Skamarock et al. 2019), which is fully compressible and nonhydrostatic. The domain is periodic in x and y directions, 9810 km long and 198 km wide with a 3 km horizontal grid spacing. A single y -invariant ridge is present. It uses 38 hybrid terrain-following/pressure vertical levels stretching from the surface to 112 hPa, corresponding to about 16 km. The domain length is chosen so the flow fully recovers to an undisturbed state after encountering the mountain ridge, before circling back in the periodic domain. Comparisons of its vertical structure 3000 km upstream (or, equivalently 6810 km downstream) of the ridge with a flat, ocean-covered simulation (not shown) shows no appreciable difference, confirming the domain length is sufficient. The y dimension is large enough for several convective clouds of sizes $O(1 - 10)$ km to develop in that cross-stream direction. The 3 km grid spacing is a compromise between the need for realistic simulation of convection and the computational cost of long time integrations. This resolution has been widely

used in large-domain convection-permitting simulations (Satoh et al. 2019), including geometries similar to ours (Wing and Cronin 2016; Wang and Sobel 2017). Kirshbaum (2020) found that in idealized cases of mechanically forced orographic convection (though at smaller spatial scales and time scales) with interactive surface fluxes (i.e., their MECH-FLX simulations), a resolution of 2 km gave similar along-stream precipitation profiles to runs at much smaller grid spacing $O(100$ m). Zhang and Smith (2018) found that resolutions of 2 km vs 6 km made little difference in simulating orographic convection over the Western Ghats.

Surface elevation is

$$h(x) = \begin{cases} \frac{h_0}{2} \left(1 + \cos\left(\pi \frac{x}{l_0}\right)\right) & \text{if } |x| < l_0, \\ 0 & \text{otherwise,} \end{cases} \quad (19)$$

where $l_0 = 100$ km (which yields a similar topography to a Witch-of-Agnesi ridge of half-width 50 km). Hereafter, x runs from -4405 km to 4405 km with the mountain at $x = 0$. Such one-dimensional terrain forces all parcels to ascend the ridge, rather than detouring around it, but provides a first step towards better understanding the interaction of deep convection with orography. The mountain's surface (i.e., where $|x| < l_0$) is covered with land. To obtain a closed surface energy budget and avoid having to choose a surface temperature lapse rate, the land surface is parameterized with the NoahMP scheme (Niu et al. 2011; Yang et al. 2011) using a no-flux bottom boundary condition. The rest of the domain is ocean-covered with fixed sea-surface temperature of 300 K.

The Coriolis force is applied to deviations from a uniform geostrophic wind $u_0 = -10$ m s⁻¹ (i.e., an easterly wind), with fixed Coriolis parameter $f = 4.97 \cdot 10^{-5}$ s⁻¹ (corresponding to 20°N). This is equivalent to imposing a background meridional pressure gradient, which maintains a constant background geostrophic flow. Microphysics are computed using the single-moment Thompson et al. (2008) scheme, surface layer mixing employs the MM5 similarity theory (Jiménez et al. 2012), and boundary layer fluxes are parameterized with the Mellor-Yamada-Janjić scheme (Mellor and Yamada 1982; Janjić 2002). The model is run without a turbulence scheme (although the surface layer and PBL schemes do parameterize turbulent mixing), but comparing the first 20 days of simulation with a run having nonzero turbulent diffusion does not show any appreciable difference. Radiation is computed interactively every minute with the RRTMG scheme (Iacono et al. 2008). All simulations have a diurnal cycle of insolation but no seasonal cycle (the solar declination angle is fixed to 0°, a state of perpetual equinox).

We perform two “control” simulations, one with mountain height $h_0 = 1000$ m and the other with $h_0 = 500$ m. The first case is close to several mountain ranges of South Asia (Western Ghats, Annam Range, Arakan Yoma) and yields

a nondimensional mountain height $Nh_0/u_0 \approx 1.2$, which suggests moderate flow blocking by the ridge: flow could be forced to split if the mountain were not infinite (Smith 1989). The second case is perhaps a better test for the linear theory, exhibiting reduced blocking ($NH/u_0 = 0.6$). Both are integrated for 200 days with statistics collected after spinup of 50 days.

An additional simulation with $h_0 = 1000$ m is run with latent heating turned off (the “ $L_v = 0$ simulation”) to assess the effect of the mountain on the flow in the absence of moist convection. It is initialized with mean temperature and moisture soundings from the control and run for 100 days, with radiation and surface fluxes turned off. Water can still condense and fall, and virtual temperature effects are retained. The temperature profile warms in the boundary layer by about 3 K in this run, but sees little change aloft; the vertical profile of N , which controls the mountain-induced dry gravity wave (Durran 2003), is little altered.

b. Precipitation and CAPE

Meridionally averaged and time averaged (from days 50 to 200) precipitation and CAPE from the $h_0 = 500$ m and 1000 m runs are shown in Figure 3. Here, and subsequently, the x -axis is oriented so the background wind flows left to right; i.e. East is on the left, and West on the right. P_n denotes precipitation in the n m run. Both CAPE and precipitation are nearly constant more than 4000 km downstream of the mountain peak and more than 1500 km upstream. This, together with the absence of mean upward motion in that region (not shown), indicates a state of RCE far from the mountain. This supports our claim that the periodic domain is long enough for the flow to recover from the disturbance imparted by the ridge.

The general shape of the precipitation profiles are in good agreement with those from the linear theory (compare Figures 2 and 3a). Upstream-averaged precipitation (i.e., from 2000 to 5000 km upwind of the peak) is about $P_0 = 4.5$ mm day $^{-1}$ for both runs. The orographic enhancement exceeds 1 mm day $^{-1}$ starting 670 km and 720 km upstream for P_{500} and P_{1000} , respectively. The length scale of this upstream enhancement is an order of magnitude larger than typically observed in midlatitudes (e.g., Smith and Barstad (2004)) or in shallow-convective tropical flows (e.g., Kirshbaum and Smith (2009)). It is consistent with observational profiles from Figure 1. Both runs have pronounced rainfall peaks (about 12 mm day $^{-1}$ and 20 mm day $^{-1}$, respectively) on the upwind mountain slope, about 55 km upstream of the peak (slightly upwind of the maximum slope). In the rain shadow region, the negative anomalies are smaller in the $h_0 = 500$ m run than in the $h_0 = 1000$ m run, as expected from the linear theory. Both runs return to the background value P_0 around the same location, 2000 km downstream. Unlike the linear runs

with a Witch-of-Agnesi profile, there is no clear overshoot past P_0 downstream. This is mostly due to the different mountain shapes employed, as we will see that this overshoot vanishes when applying (12) to the shape (19) in part 4b. A curious feature in both runs is the presence of a small rainfall peak immediately downstream of the ridge. This is explained by a hydraulic jump at this location, as mentioned by Kirshbaum et al. (2018); it results from dry nonlinear dynamics, and its small amplitude and limited spatial extent render it incidental here.

Under the assumptions of linearity made in section 2c, changing the mountain height should scale the orographically modified precipitation proportionately, so $P_{1000} - P_0 = 2(P_{500} - P_0)$. Figure 3 shows this prediction for P_{1000} , simplified to $(2P_{500} - P_0)_+$ alongside the simulated P_{1000} . There is remarkable agreement, with the prediction lying within the uncertainty bounds of P_{1000} at nearly all locations. This provides confidence in the relevance of linear theory to mechanically forced orographic convection (we compare with our theory in detail in Section 4).

Examination of the diurnal cycle of precipitation in the $h_0 = 1000$ m run can serve as a probe of the importance of thermal forcing for convection. Between the mountaintop and 200 km upstream, the diurnal cycle of precipitation has an amplitude of 20% of the time-mean value. This is smaller than in the RCE part of the domain, where the relative amplitude is 25%, and suggests a small role for island surface fluxes in producing rainfall. For comparison, Wang and Sobel (2017) simulated thermally forced convection over isolated islands and reported relative amplitudes of the diurnal cycle of around 80%.

We also show CAPE in Figure 3 to illustrate the difficulty of using CAPE-based closures in theory for orographic precipitation. Despite the cooling effect of the gravity wave on the lower free troposphere upstream of the mountain (analyzed in more detail in Section 4c), CAPE gradually decreases starting 1000 km upstream and drops to almost zero above the mountain. This can be understood as a progressive consumption of CAPE by enhanced convection, triggered by reduced convective inhibition (CIN; Ahmed et al. (2020) highlight the similarity of the $q - T$ closure to CIN-based convective parameterizations). Downstream of the ridge, reduced convection allows CAPE to build and even overshoot its upstream value, much like the linear theory for precipitation (Figure 2). CAPE-based closures typically diagnose precipitation as the ratio of CAPE to a convective time scale; the latter would have to vary spatially here to accommodate the absence of proportionality between CAPE and P. The time scale would have to decrease upstream of and above the mountain (e.g., due to orography “triggering” convection by mechanical forcing) and increase downstream. The challenge of such an approach is that the rainfall profile is highly sensitive to spatial variations of the time scale, rendering derivation of a physically based closure difficult.

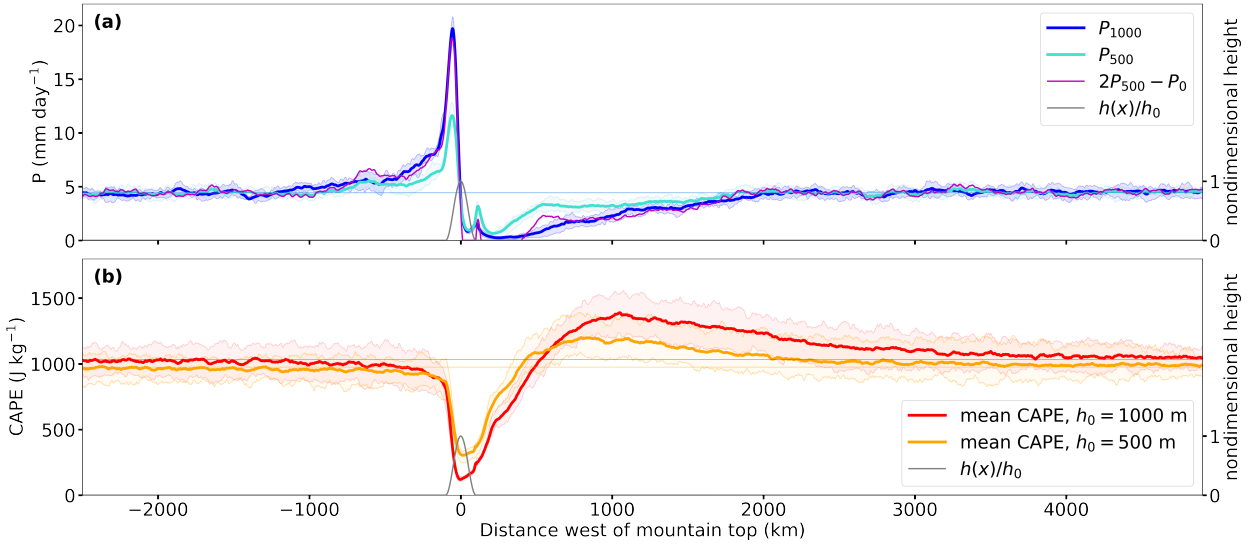


FIG. 3. Time and meridional mean precipitation (a) and CAPE (b) in the $h_0 = 500 \text{ m}$ and 1000 m runs. Thin horizontal lines indicate the upstream-averaged (between $x = -2500 \text{ km}$ and -3000 km) values. The magenta line in panel a shows the result of doubling the orographically-modified part of the precipitation ($P - P_0$) in the $h_0 = 500 \text{ m}$ run. Shadings show the interquartile ranges, as computed from binning each quantity into meridional and 10-day means at each longitude.

c. Vertical motion

Figure 4 shows time and meridionally averaged vertical velocity in the $h_0 = 1000 \text{ m}$ control run and the $L_v = 0$ run. Interaction of the basic state flow with the mountain produces a gravity wave in the $L_v = 0$ run that influences the flow between about 500 km upstream and 2000 km downstream of the mountain, beyond which the wave amplitude decays to less than 0.01 m s^{-1} . Vertical motion in the control run strongly resembles that in the $L_v = 0$ run from 200 km upstream to 1000 km downstream of the ridge¹. Further upstream (between $x = -1000 \text{ km}$ and -200 km), deep ascent is visible in the time-mean, suggesting that enhanced precipitation in this region is due to a feedback of moist convection on the mountain-induced low-level ascent.

The similarity between the dry and moist w above the ridge raises the question of how much precipitation the dry wave would produce without moist convective feedback. The $L_v = 0$ simulation does produce precipitation in its initial times, before moisture has been depleted (there are no surface fluxes in that run). This precipitation is focused on the upwind slope only, and could be of comparable magnitude to the control run in that region if moisture was constantly replenished. Taking this effect into account in

the theory would only have a slight impact because the dry forcing (through q_{dL}) would decrease by a compensating amount, leaving total precipitation nearly unchanged.

To illustrate the dynamics producing rainfall over the ridge, we plot the instantaneous vertical velocity at 500 hPa at a rainy time in Figure 5. Vertical motion over the upwind slope is composed of isolated deep convective cells (extending to 200 hPa, not shown) surrounded by cold pools, qualitatively similar to cells observed upstream over ocean. This contrasts with the classic, midlatitude-centric view of laminar mountain ascent producing the bulk of precipitation. This justifies our approach of developing a theory for orographic precipitation based on the behavior of an ensemble of convective motions. Past the mountaintop, convective motions are absent, consistent with the lack of precipitation there.

d. Thermodynamic equation

We now evaluate the degree to which the linearization we employed as our starting point in (1a)-(1b), as well as WTG, are valid approximations.

Figure 6a shows vertically averaged terms from the thermodynamic equation (A1a) and its linearized version (1a), computed using time and meridional mean quantities (denoted with an overbar). Diabatic heating is computed as a residual and plotted with precipitation (or rather gP/P_T) for comparison. The diagnosed diabatic heating underestimates precipitation immediately downstream of its peak, but shows very good agreement upstream. The linearized terms (i.e., replacing \mathbf{u} and s by $\overline{\mathbf{u}}_0$ and \overline{s}_0) closely match

¹A simple scale analysis explains the prominence of the “dry” gravity wave in the moist simulation. Dry vertical motion scales as $w_{\text{dry}} \sim u_0 \frac{dh}{dx} \approx 0.15 \text{ m s}^{-1}$, while the diabatic w scales as $w_{\text{diabatic}} = Q_c / \frac{ds_0}{dz} = (gP/P_T)/(C_p T_0 N^2/g) \approx 0.024 \text{ m s}^{-1}$, using $P = 20 \text{ mm day}^{-1}$ (multiplied by $\rho_w L_v$), $T_0 = 300 \text{ K}$ and $N = 0.01 \text{ s}^{-1}$. Hence, gravity wave dynamics are expected to dominate over the ridge unless time-mean P increases by an order of magnitude.

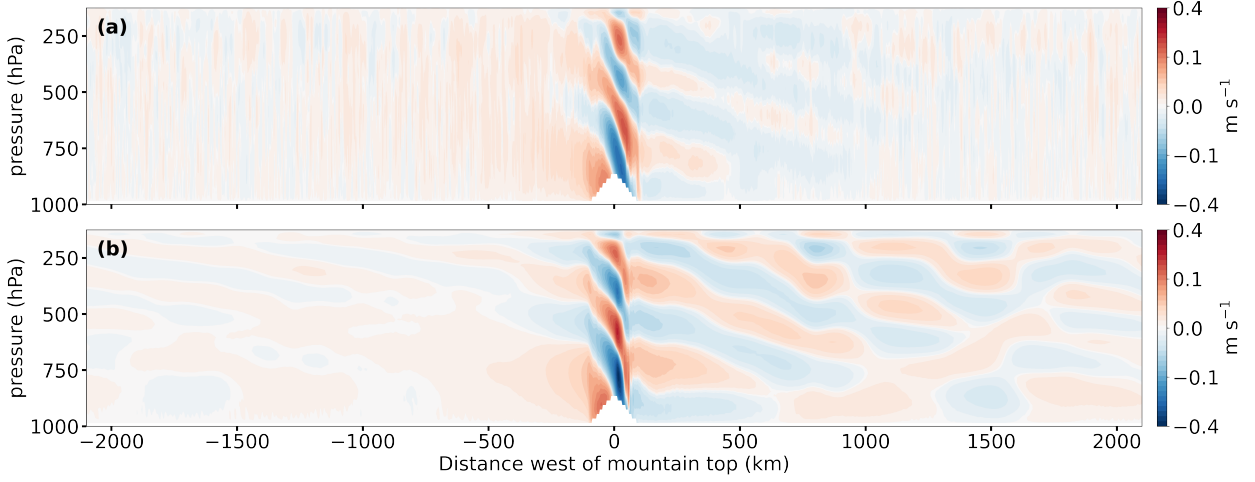


FIG. 4. Time and meridionally-averaged vertical velocities from the $h_0 = 1000$ m control run (a) and $L_v = 0$ run (b). Note the nonlinearity of the color scale.

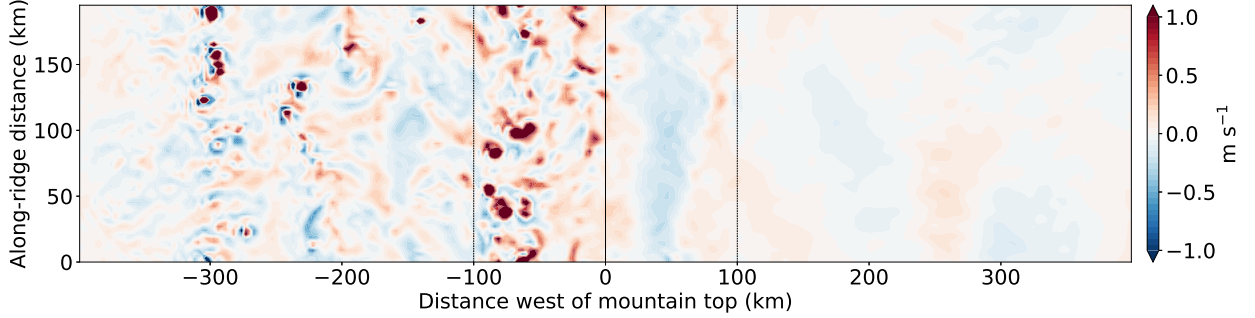


FIG. 5. Instantaneous vertical velocity at 500 hPa in the vicinity of the mountain, from the $h_0 = 1000$ m run, day 150, 19h.

the “full” terms except between 30 km upstream to 100 km downstream of the peak. Much of the precipitation is concentrated upwind of this region, where it is accurately matched by the diabatic heating diagnosed from linearized terms. Between $x = -30$ km and $x = +100$ km, the small diabatic heating indicates that the disagreement between linearized and full terms is unlikely to be due to moist effects, and rather due to the nonlinear part of the dry mountain wave.

We now turn to validation of the WTG assumption. The good match between linearized temperature advection terms from the $h_0 = 1000$ m simulation (i.e., $\langle \mathbf{u}_0 \cdot \nabla (\bar{T}_d + \bar{T}_m) \rangle$) and from the $L_v = 0$ simulation ($\langle \mathbf{u}_0 \cdot \nabla \bar{T}_d \rangle$), shown in Figure 6b, ensures that $|\mathbf{u}_0 \cdot \nabla T_m| \ll |\mathbf{u}_0 \cdot \nabla T_d|$. The smallness of the dry residual $\langle \mathbf{u}_0 \cdot \nabla \bar{T}_d + \bar{\omega}_d ds_0/dp \rangle$ indicates that the dry linearized thermodynamic budget holds. Taken together, these indicate that $\langle \bar{\omega}_m ds_0/dp \rangle \approx \langle \bar{Q}_c \rangle + \langle \bar{R} \rangle$, which is exactly the WTG approximation.

4. Comparing theory and simulations

Precipitation profiles from the convection-permitting numerical simulations are now used as a first test of our theory. We compare these profiles against both the linear theory (12) and the nonlinear one (6), with the dry forcing for the latter extracted from the simulations. We will show that while precipitation profiles are well-captured by the theory, their upstream amplitude is overestimated. This issue is addressed by modifying the adjustment time scales to values appropriate for seasonal means. A last adjustment incorporates the downstream modulation of evaporation and radiative cooling to (6).

a. Temperature and moisture deviations

We first examine lower-tropospheric temperature and moisture perturbations of the dry mode, which drive convection in (6), and compare these to predictions of the linear theory (obtained by combining (7) and (11)).

Figure 7 shows T'_L and q'_L from the $h_0 = 1000$ m control and $L_v = 0$ runs. These are time-averaged, meridional-

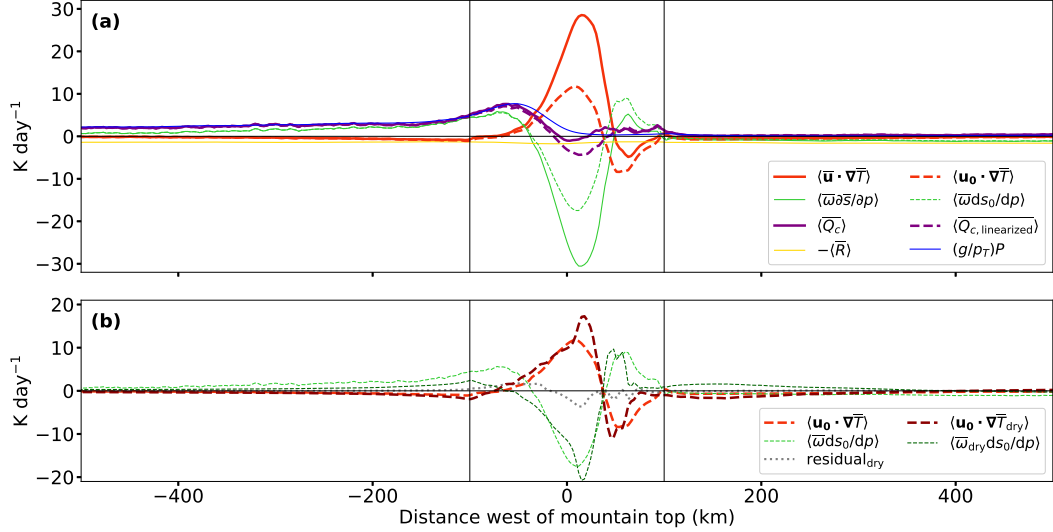


FIG. 6. Vertically averaged thermodynamic budget terms. Panel a shows ‘full’ (nonlinear) terms for the $h_0 = 1000 \text{ m}$ control run, as well as their linearized version (obtained by fixing \mathbf{u} and s to their basic state values). The simulated precipitation rate is shown in blue for comparison. Panel b focuses on the linearized heat advection and adiabatic cooling terms, comparing the $h_0 = 1000 \text{ m}$ control and $L_v = 0$ runs. The vertical black lines show the extent of the mountain.

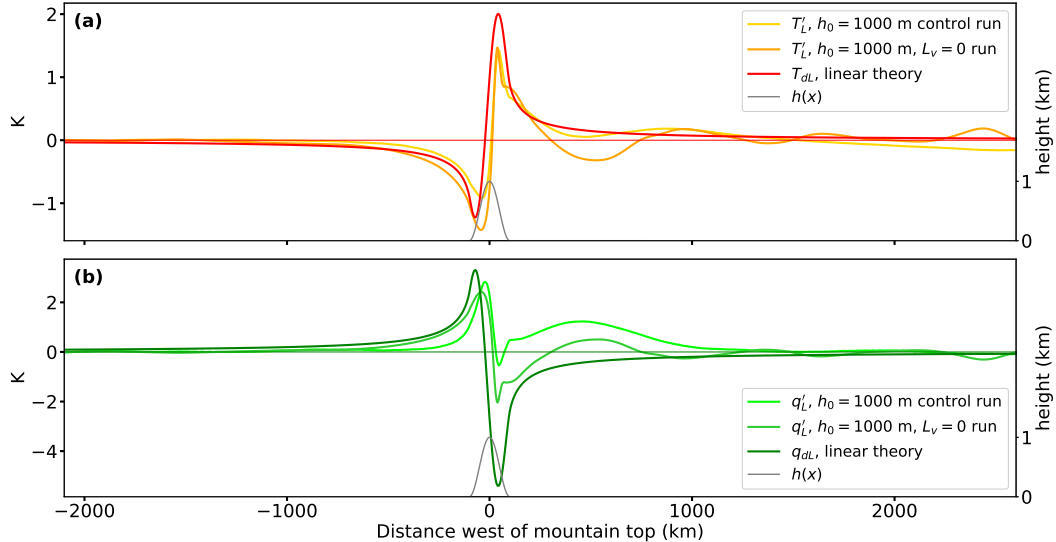


FIG. 7. Profiles of lower-tropospheric averaged temperature (a) and moisture (b) perturbations relative to 3000 km upstream in the $h_0 = 1000 \text{ m}$ control and $L_v = 0$ simulations, as well as perturbations computed from the linear theory ((7) and (11)).

averaged, and pressure-averaged (875 hPa to 700 hPa) deviations from a mean sounding 3000 km upstream of the mountaintop. Under our WTG assumptions, $T'_L = T_{dL}$, so we also plot T_{dL} as predicted by linear mountain wave theory with $N = 0.01 \text{ s}^{-1}$. The agreement is generally good, especially given our neglect of nonlinearity of the dry mountain wave, shown to be important above the peak in Figure 6. However, upstream of the mountain, T'_L in the control run is about a third smaller in magnitude than in the $L_v = 0$ run. What could explain this? Remember that

T_{dL} can be approximated from (7) as

$$T_{dL}(x) = -\frac{1}{u_0} \int_{-\infty}^x \left(w_d \frac{ds_0}{dz} \right)_L dx'. \quad (20)$$

Upstream of the mountain, w_d has a larger amplitude in the control run than in the $L_v = 0$ run, which cannot explain the discrepancy. A possible explanation for the smaller upstream magnitude of T'_L in the control run is that the dry mode feels a reduced static stability, due in part to ascent occurring moist adiabatically (O’Gorman 2011).

This would challenge our assumption that the dry mode is unaffected by the moist mode, and is left as potential improvement for future work.

q'_L is an equally important modulator of convection to T'_L , and is also shown in Figure 7. We do not expect the control and $L_v = 0$ runs to produce similar distributions of q_L : q_{mL} is expected, upstream, to be reduced by the precipitation forced by the dry mode, which happens as expected. Linear theory (with the same moisture lapse rate as in section 2d) matches q_{dL} upstream of the mountain peak except its peak value being too high, and overestimates orographic wave-induced drying downstream. Moisture depletion at the beginning of the dry run (see section 3c) may explain this discrepancy, as q_{dL} is evaluated from the last 50 days of the $L_v = 0$ run.

Altogether, these results suggest that linear theory (12) will estimate upstream distribution of precipitation nearly as accurately as the nonlinear theory (6) forced by the simulated q_{dL} and T_{dL} . One might expect the linear theory to yield a higher magnitude, due to an overestimated temperature decrease, if a reduced effective static stability is not used. Several elements are expected to affect predictions of the linear theory in the rain shadow: the overestimated subsidence-induced drying, and the neglect of the constraint that convective heating be non-negative.

b. Precipitation

Figure 8a displays the application of linear theory (12) to the mountain profile (19) used in the simulations, with $h_0 = 1000$ m. We use the same parameters as in section 2d, except choosing $P_0 = 4.5 \text{ mm day}^{-1}$ to match the simulations (see section 3b). We keep $M_s/M = 5$ henceforth². Linear precipitation reaches a peak of 50 mm day^{-1} on the upwind flank of the ridge, substantially higher than the linear theory produced for the Witch of Agnesi profile (Figure 2) because of the steeper ascent imposed by (19). A more gradual ascent provides a greater distance for P to relax back to P_0 (first term on the right-hand side of (6)).

As an intermediate level of complexity between linear theory and the convection-permitting simulations, Figure 8a displays mean precipitation computed from equation (6). The dry forcing required by (6) is obtained by taking T_{dL} from the $h_0 = 1000$ m control simulation and q_{dL} from the $L_v = 0$ simulation (see Figure 7). Downstream of the mountain, q_{dL} oscillates in a way not seen in the dry mode of the control run (owing to the smaller amplitude of the orographic lee wave, see Figure 4), but we did not correct for this. All other parameters are the same as above, and (6) is integrated numerically with a backward differentiation formula method. As expected from the profiles in Figure 7, precipitation computed this way

compares well with linear theory, except for a peak that is smaller and shifted modestly downstream. Two effects explain the differences between precipitation rates computed from (6) and (12) downstream of the mountain. First, oscillations in the precipitation rate, including a weak local maximum between 400 km and 600 km downwind of the mountain peak, are due to the shapes of q_{dL} and T_{dL} in the convection-permitting simulations. The second effect is due the Heaviside function in (6), which increases the length of non-precipitating regions; forbidding negative values of P reduces the recovery rate $(P_0 - P)/L_q$, so that P converges towards P_0 more slowly.

The linear and nonlinear theories both overestimate the precipitation rate by a factor of two or three compared to the convection-permitting simulation, which has a peak of 20 mm day^{-1} . We hypothesize that this occurs because increased adjustment time scales (τ_q and τ_T) are needed when applying the theory to seasonal-scale time means. Spatio-temporal averaging of the convective heating term (3) necessarily includes non-convective regions and times, yielding higher effective adjustment scales (see Ahmed et al. 2020). To rescale τ_q and τ_T , we compute the time- and meridional-mean rain rate excluding non-precipitating times (Appendix B provides details). Excluding non-precipitating periods doubles the rain rate, thus doubling P' (i.e. $P_{1000} - P_0$). The theoretical P' is, in the upstream region, inversely proportional to the adjustment scales because (6) is linear in that region where $P > 0$. This suggests that accounting for non-precipitating times requires doubling τ_q and τ_T , compared to the “instantaneous” values estimated by Ahmed et al. (2020).

The simulated mean precipitation is best fit by increasing both adjustment times 2.5-fold (yielding $\tau_T = 7.5$ hours and $\tau_q = 27.5$ hours), near the factor of 2 expected from excluding non-precipitating times from the time-average (see above and Appendix B). Figure 8b,c shows the revised prediction for linear and nonlinear theories and both mountain heights. For the nonlinear theory applied to the $h_0 = 500$ m run, T_{dL} is taken directly from the $h_0 = 500$ m run, while q_{dL} is taken as half of q_{dL} from the $L_v = 0$ run with $h_0 = 1000$ m (due to the absence of a $h_0 = 500$ m, $L_v = 0$ run). Nonlinear theory agrees well with the simulated precipitation upstream of the mountain, for both mountain heights, while linear theory still overestimates peak rain rates. The linear theory fit might be improved by accounting for a lower effective static stability (as explained in section 4a), but we did not attempt this.

c. Surface evaporation and radiative cooling in the rain shadow

Using the nonlinear theory with increased time scales overestimates the simulated precipitation downstream of the mountain (Figure 8b,c), possibly because the theory neglects variations in evaporation and radiative cooling

²Indeed, following the method outlined by Yu et al. (1998), we estimate $M_s = 2370 \text{ J kg}^{-1}$ and $M_h = 455 \text{ J kg}^{-1}$ in the $h_0 = 1000$ m run (respectively 2341 J kg^{-1} and 450 J kg^{-1} in the $h_0 = 500$ m run).

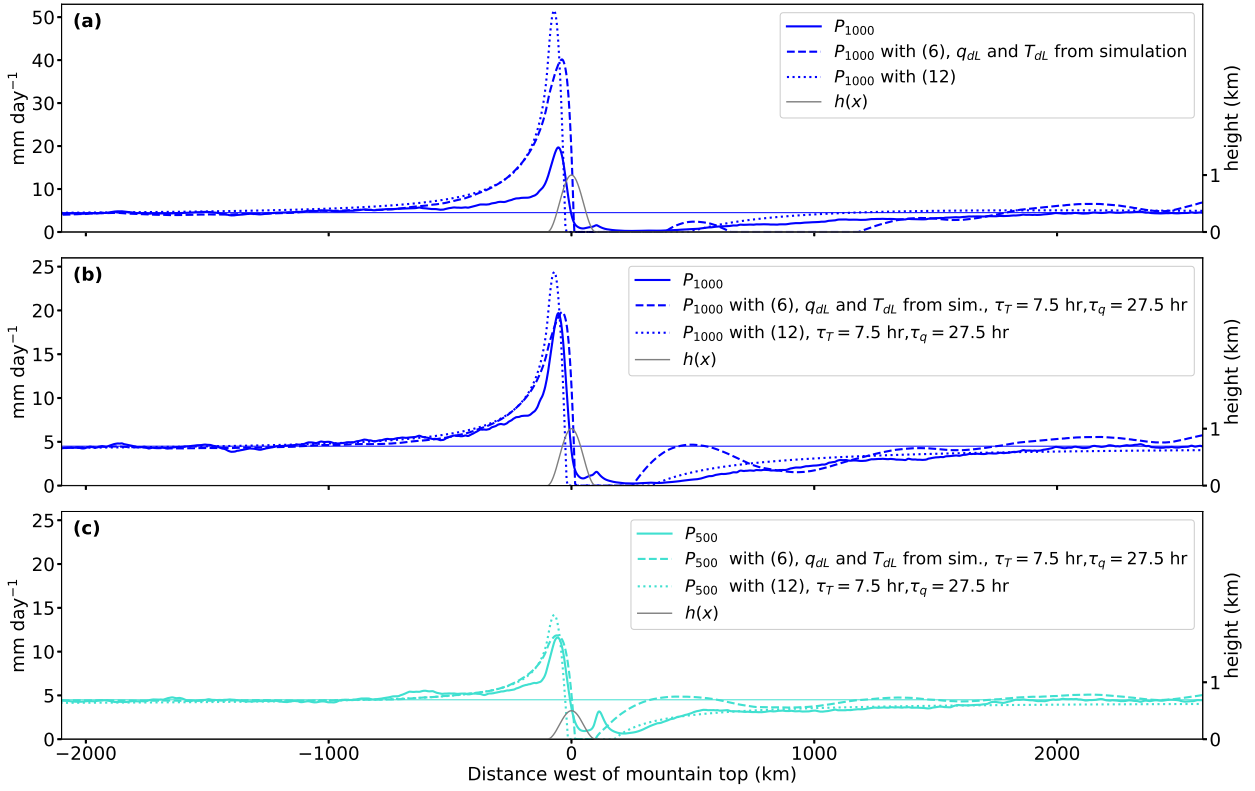


FIG. 8. Profiles of mean precipitation rates over 1000 m high (a and b) and 500 m high (c) mountains. Solid lines are simulated rates, dashed lines are computed from the nonlinear theory (6) with lower-tropospheric perturbations q_{dL} and T_{dL} diagnosed from simulations (see text), and dotted lines are profiles from the closed linear theory (12). The convective adjustment scales are taken from Ahmed et al. (2020) (a), then increased 2.5-fold (b and c). The thin horizontal lines show P_0 .

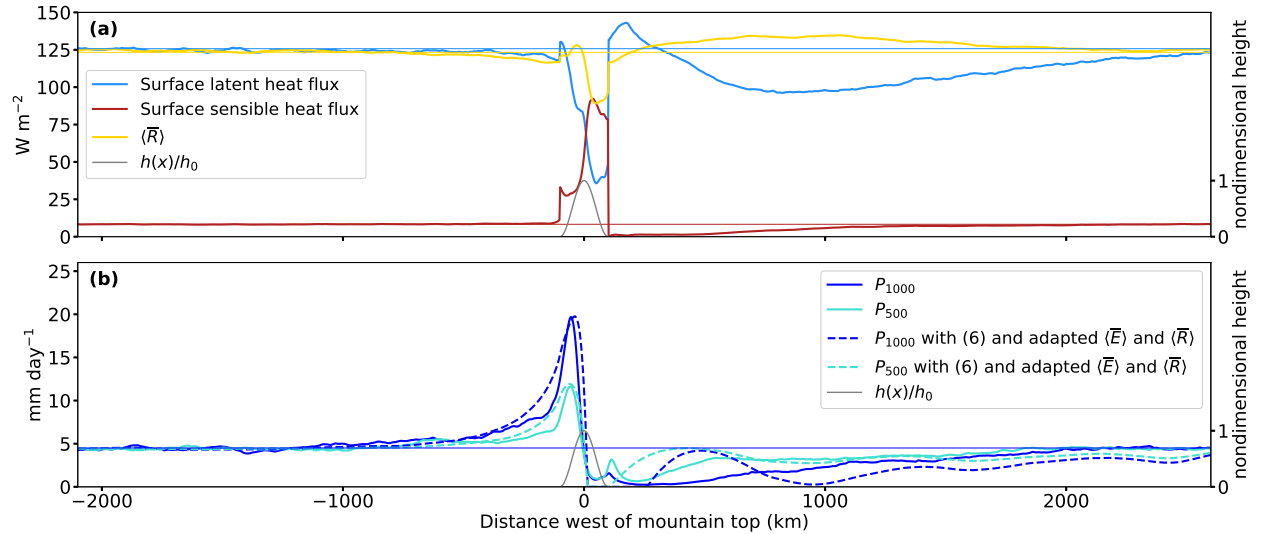


FIG. 9. (a) Time and meridionally averaged surface fluxes and radiative cooling from the $h_0 = 1000$ m simulation. Thin horizontal lines indicate the upstream-averaged (between -2500 km and -3000 km) values. (b) As in Figure 8b,c, without solutions from (12), and where solutions from (6) take into account spatial variations in evaporation and radiative cooling.

(i.e., it assumes P_0 is uniform). Profiles of $\langle E \rangle$, $\langle R \rangle$, and the surface sensible heat flux are shown in Figure 9a. Although the upstream region is in RCE, the sum of surface fluxes appears to not match radiative cooling there because the former are computed as averages of 6-hourly output, whereas the latter is accumulated at each time step.

The starker deviations from the constant upstream values occur above the mountain and 100 km to 2000 km downwind of the mountaintop. A strong reduction in evaporation above the ridge, which is covered with land, is largely compensated by increased sensible heating. Downstream, evaporation increases over a 200 km-long region before decreasing to 80% of its upstream value. This decrease can be attributed (not shown) to increased near-surface relative humidity, likely caused by suppressed convection in that region. Suppressed convection also reduces the occurrence of high clouds and, as a consequence, increases radiative cooling by up to 10% downstream. Earlier theory (e.g. Fuchs and Raymond 2002) parameterized this effect with a feedback factor, setting $\langle R' \rangle$ proportional to P' (where $\langle R' \rangle$ denotes radiative cooling minus its RCE value).

The downstream modulation of $\langle E \rangle$ and $\langle R \rangle$ strongly decreases P_0 , according to (5). Accounting for this in (6) nearly halves the computed rain rate downstream, as shown in Figure 9b. Incorporating a closure for $\langle E \rangle$ and $\langle R \rangle$ into our theory, rather than diagnosing these from simulations, is left for future work.

5. Summary and conclusions

We present a theory of convective precipitation forced by the mechanical effects of orography at low latitudes. It starts with decomposition of the flow into the sum of a dry mode, carrying the orographic gravity wave, and a moist mode bearing the convective response. Precipitation is assumed to be produced entirely by the moist mode, whose dynamics are vertically truncated and subject to the WTG approximation. Convective heating responds to lower-tropospheric temperature and moisture perturbations carried by both modes in a quasi-equilibrium framework. Two degrees of complexity can be employed. The first consists of computing the dry mode perturbations with a numerical model for use in the theory, with the theory retaining the nonlinearity of the convective closure. The second option neglects this nonlinearity and assumes linear mountain wave dynamics to derive a linear model of convective orographic rainfall much in the spirit of the Smith and Barstad (2004) midlatitude model. The linear theory provides analytical solutions to probe the sensitivity of maximum precipitation, upstream extent of precipitation enhancement, and rain-shadow length to the physical parameters at play, namely upstream wind, convective adjustment scales, relative GMS, static stability, and moisture lapse rate.

This theory describes time-mean rainfall in tropical orographic regions, and assumptions related to the vertical structure of the moist mode and WTG prevent its use in midlatitudes. Its applicability to short-term precipitating events is also questionable, owing to the unsuitability of the QE assumption at these time scales. It does not account for cloud delays nor the advection of hydrometeors, although we believe these could be added to the linear version without much difficulty. Most importantly, the model is not suited to the description of thermally forced orographic convection.

The theory is tested against convection-permitting simulations in long-channel geometry. The dry orographic gravity wave is prominent in the moist model, justifying its consideration as a driver of terrain-generated convection. After correcting adjustment time scales to account for the effects of seasonal averaging, the theory accurately reproduces precipitation rates simulated by this model, especially upstream of the mountain peak. The linear version is skillful at modeling dry temperature and moisture deviations, and hence precipitation, upwind of the ridge. The mountain alters evaporation and radiative cooling far downstream, reducing rainfall there.

This theory is envisioned as a tool for understanding the spatial variability of rainfall in tropical orographic regions where mechanical forcing prevails. Examples include South Asia and Mexico during their respective summer monsoons, or most tropical land regions subject to an autumn monsoon (Ramesh et al. 2021). Understanding the interaction of large-scale flow with orography in such regions is key to comprehending past variability in tropical rainfall, as well as predicting changes in coming decades. The theory could also be used to probe the importance of orography in shaping large-scale tropical circulations through its influence on moist convection.

Acknowledgments. This material is based on work supported by the U.S. Department of Energy, Office of Science, Office of Biological and Environmental Research, Climate and Environmental Sciences Division, Regional and Global Model Analysis Program, under Award DE-SC0019367. It used resources of the National Energy Research Scientific Computing Center (NERSC), which is a DOE Office of Science User Facility. QN acknowledges support from the McQuown fund at UC Berkeley. The authors wish to thank Daniel Kirshbaum for very helpful feedback and suggestions.

Data availability statement. Processed WRF output and code used in producing the figures will be archived at Zenodo, with a DOI issued once the review process and any needed revisions are complete. Raw WRF output is available from the authors upon request (qnico-las@berkeley.edu), and TRMM and ERA5 data are publicly accessible online.

APPENDIX A

Decomposition into dry and moist modes

We describe flow around a tropical mountain as the sum of a dry mode (representing the influence of orography in the absence of condensation) and a moist convective one. The dry mode affects the moist mode through convective heating, but the moist mode does not feed back on the dry mode. Steady-state thermodynamic and moisture equations are

$$\mathbf{u} \cdot \nabla T + \omega \frac{\partial s}{\partial p} = Q_c - R, \quad (\text{A1a})$$

$$\mathbf{u} \cdot \nabla q + \omega \frac{\partial q}{\partial p} = Q_q + E, \quad (\text{A1b})$$

with notation as in section 2a. Wind, moisture and temperature are decomposed as follows:

$$\begin{aligned} \omega &= 0 + \omega_d + \omega_m, \\ \mathbf{u} &= \mathbf{u}_0 + \mathbf{u}_d + \mathbf{u}_m, \\ q &= q_0(p) + q_d + q_m, \\ T &= T_0(p) + T_d + T_m, \end{aligned} \quad (\text{A2})$$

where subscripts *d* and *m* denote dry and moist modes, respectively.

We now linearize (A1a)-(A1b) about a state of uniform horizontal wind \mathbf{u}_0 , zero vertical velocity, and horizontally uniform dry static energy $s_0(p)$ and specific humidity $q_0(p)$. We justify this approach based on scales estimated from the $h_0 = 1000$ m control and $L_v = 0$ simulations. For horizontal advection terms, we exploit the fact that the strong basic state wind \mathbf{u}_0 dominates the horizontal wind dynamics, i.e. $|\mathbf{u}_d|, |\mathbf{u}_m| \ll |\mathbf{u}_0|$. The assumption $|\mathbf{u}_m| \ll |\mathbf{u}_0|$ is well justified as the standard deviation of \mathbf{u} is less than 2 m s^{-1} in the RCE region of our convection-permitting simulations. In those simulations, we also find $|\mathbf{u}_d| \ll 0.3|\mathbf{u}_0|$, except right above the mountain where the orographic gravity wave disrupts the flow substantially. In section 3d, we show that such nonlinearity in the dry dynamics does not seem to affect the moist mode dynamics, despite its local importance in the thermodynamic budget.

For vertical advection terms, we assume $\partial s_d/\partial p, \partial s_m/\partial p \ll \partial s_0/\partial p$. Again, this is supported by the simulations except for the dry perturbations right above the mountain. In height coordinates, $\partial s_0/\partial z \approx 4 \text{ K/km}$, and deviations above the mountain in the $L_v = 0$ simulation give $|\partial s_d/\partial z| \lesssim 1 - 2 \text{ K/km}$. Static stability variations from the moist mode are at least two orders of magnitude smaller than the basic state static stability (see Neelin and Zeng 2000).

Using these approximations, (A1a)-(A1b) become

$$\mathbf{u}_0 \cdot \nabla T_d + \omega_d \frac{\partial s_0}{\partial p} + \mathbf{u}_0 \cdot \nabla T_m + \omega_m \frac{\partial s_0}{\partial p} = Q_c - R, \quad (\text{A3a})$$

$$\mathbf{u}_0 \cdot \nabla q_d + \omega_d \frac{\partial q_0}{\partial p} + \mathbf{u}_0 \cdot \nabla q_m + \omega_m \frac{\partial q_0}{\partial p} = Q_q + E. \quad (\text{A3b})$$

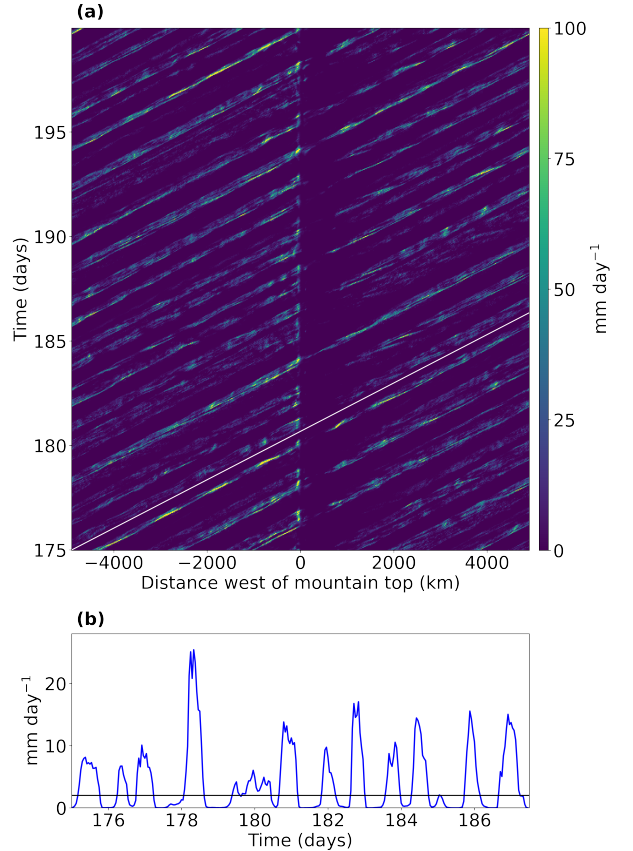


FIG. B10. (a) Hovmöller diagram of precipitation rate in the $h_0 = 1000$ m run (in the x - t plane). An example characteristic line ($L_{175\text{days}}$) is shown in white. (b) Precipitation averaged over characteristic lines. The x -axis shows the time at which a characteristic line starts, at $x_0 = -4905$ km. The solid black line denotes the threshold defining a precipitating characteristic (2 mm day^{-1}).

The first two terms in each equation (the dry mode) balance each other, expressing conservation of potential temperature and moisture in the dry perturbation. Note that Q_q could potentially be nonzero in the dry mode (i.e., some moisture could condense and fall, even in the absence of latent heating), but this effect is confined to the upwind mountain slope in the $L_v = 0$ run (consistently with Zhang and Smith (2018)); further discussion is provided in section 3c. Accounting for the dry mode balance in (A3a)-(A3b) yields (1a)-(1b).

APPENDIX B

Selection of precipitating times

To justify the increase in adjustment time scales needed to represent seasonal-mean dynamics, we show how the exclusion of non-precipitating times leads to a doubling

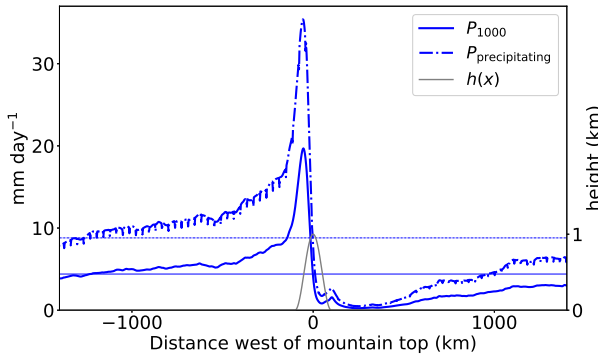


FIG. B11. Rain rate averaged over precipitating times only (see text), and all-time mean rain rate, for the $h_0 = 1000$ m run.

of the time-mean rain rate. Rainfall in the $h_0 = 1000$ m and 500 m simulations is produced by a variety of convective systems (e.g. Figure 5) propagating near velocity \mathbf{u}_0 . Figure B1a shows a Hovmöller diagram of meridionally averaged precipitation over days 175–200 in the $h_0 = 1000$ m simulation. We average precipitation over characteristic lines $L_t = (t, x(t) = x_0 + u_0 t)$ with $x_0 = -4905$ km and t running from days 50 to 188 (the last time for which the whole characteristic line is included in the domain) in hourly samples. The resulting $P_{\text{characteristic}}(L_t)$ is plotted for days 175–188 on Figure B1b. The mean rainfall over precipitating times, $P_{\text{precipitating}}$, is then computed as the average over characteristic lines satisfying $P_{\text{characteristic}} > 2$ mm day^{-1} . It is displayed in figure B2, along with the all-time mean P_{1000} .

References

- Ahmed, F., Á. F. Adams, and J. D. Neelin, 2020: Deep convective adjustment of temperature and moisture. *Journal of the Atmospheric Sciences*, **77** (6), 2163 – 2186, doi:10.1175/JAS-D-19-0227.1.
- Arakawa, A., and W. H. Schubert, 1974: Interaction of a cumulus cloud ensemble with the large-scale environment, part I. *Journal of Atmospheric Sciences*, **31** (3), 674 – 701, doi:10.1175/1520-0469(1974)031<0674:IOACCE>2.0.CO;2.
- Biasutti, M., S. E. Yuter, C. D. Burleyson, and A. H. Sobel, 2012: Very high resolution rainfall patterns measured by TRMM precipitation radar: seasonal and diurnal cycles. *Climate Dynamics*, **39** (1), 239–258.
- Cannon, D. J., D. J. Kirshbaum, and S. L. Gray, 2014: A mixed-phase bulk orographic precipitation model with embedded convection. *Quarterly Journal of the Royal Meteorological Society*, **140** (683), 1997–2012, doi:10.1002/qj.2269.
- Chen, S.-H., and Y.-L. Lin, 2005: Effects of moist Froude number and CAPE on a conditionally unstable flow over a mesoscale mountain ridge. *Journal of the Atmospheric Sciences*, **62** (2), 331 – 350, doi:10.1175/JAS-3380.1.
- Chu, C.-M., and Y.-L. Lin, 2000: Effects of orography on the generation and propagation of mesoscale convective systems in a two-dimensional conditionally unstable flow. *Journal of the Atmospheric Sciences*, **57** (23), 3817 – 3837, doi:10.1175/1520-0469(2001)057<3817:EOOOTG>2.0.CO;2.
- Derbyshire, S. H., I. Beau, P. Bechtold, J.-Y. Grandpeix, J.-M. Piriou, J.-L. Redelsperger, and P. M. M. Soares, 2004: Sensitivity of moist convection to environmental humidity. *Quarterly Journal of the Royal Meteorological Society*, **130** (604), 3055–3079, doi:<https://doi.org/10.1256/qj.03.130>.
- Durran, D. R., 2003: Lee waves and mountain waves. *Encyclopedia of atmospheric sciences*, **1161**, 1170.
- Emanuel, K. A., J. David Neelin, and C. S. Bretherton, 1994: On large-scale circulations in convecting atmospheres. *Quarterly Journal of the Royal Meteorological Society*, **120** (519), 1111–1143, doi:10.1002/qj.49712051902.
- Fuchs, Ž., and D. Raymond, 2002: Large-scale modes of a nonrotating atmosphere with water vapor and cloud–radiation feedbacks. *Journal of the Atmospheric Sciences*, **59**, 1669–1679.
- Hersbach, H., and Coauthors, 2020: The ERA5 global reanalysis. *Quarterly Journal of the Royal Meteorological Society*, **146** (730), 1999–2049, doi:10.1002/qj.3803.
- Houze, R. A., 2012: Orographic effects on precipitating clouds. *Reviews of Geophysics*, **50** (1), doi:10.1029/2011RG000365.
- Huffman, G. J., and Coauthors, 2007: The TRMM Multisatellite Precipitation Analysis (TMPA): Quasi-global, multiyear, combined-sensor precipitation estimates at fine scales. *Journal of Hydrometeorology*, **8** (1), 38 – 55, doi:10.1175/JHM560.1.
- Iacono, M. J., J. S. Delamere, E. J. Mlawer, M. W. Shephard, S. A. Clough, and W. D. Collins, 2008: Radiative forcing by long-lived greenhouse gases: Calculations with the AER radiative transfer models. *Journal of Geophysical Research: Atmospheres*, **113** (D13), doi:10.1029/2008JD009944.
- Janjić, Z., 2002: Nonsingular implementation of the Mellor–Yamada level 2.5 scheme in the NCEP Meso model. *NCEP Office Note*, **436**.
- Jiménez, P. A., J. Dudhia, J. F. González-Rouco, J. Navarro, J. P. Montávez, and E. García-Bustamante, 2012: A revised scheme for the WRF surface layer formulation. *Monthly Weather Review*, **140** (3), 898 – 918, doi:10.1175/MWR-D-11-00056.1.
- Kirshbaum, D. J., 2020: Numerical simulations of orographic convection across multiple gray zones. *Journal of the Atmospheric Sciences*, **77** (10), 3301 – 3320, doi:10.1175/JAS-D-20-0035.1.
- Kirshbaum, D. J., B. Adler, N. Kalthoff, C. Barthlott, and S. Serfin, 2018: Moist orographic convection: Physical mechanisms and links to surface-exchange processes. *Atmosphere*, **9** (3), doi:10.3390/atmos9030080.
- Kirshbaum, D. J., and R. B. Smith, 2009: Orographic precipitation in the tropics: Large-eddy simulations and theory. *Journal of the Atmospheric Sciences*, **66** (9), 2559 – 2578, doi:10.1175/2009JAS2900.1.
- Mellor, G. L., and T. Yamada, 1982: Development of a turbulence closure model for geophysical fluid problems. *Reviews of Geophysics*, **20** (4), 851–875, doi:10.1029/RG020i004p00851.
- Miglietta, M. M., and R. Rotunno, 2009: Numerical simulations of conditionally unstable flows over a mountain ridge. *Journal of the Atmospheric Sciences*, **66** (7), 1865 – 1885, doi:10.1175/2009JAS2902.1.
- Miglietta, M. M., and R. Rotunno, 2012: Application of theory to simulations of observed cases of orographically forced convective

- rainfall. *Monthly Weather Review*, **140** (9), 3039 – 3053, doi:10.1175/MWR-D-11-00253.1.
- Miglietta, M. M., and R. Rotunno, 2014: Numerical simulations of sheared conditionally unstable flows over a mountain ridge. *Journal of the Atmospheric Sciences*, **71** (5), 1747 – 1762, doi:10.1175/JAS-D-13-0297.1.
- Neelin, J. D., and N. Zeng, 2000: A quasi-equilibrium tropical circulation model—formulation. *Journal of the Atmospheric Sciences*, **57** (11), 1741 – 1766, doi:10.1175/1520-0469(2000)057<1741: AQETCM>2.0.CO;2.
- Niu, G.-Y., and Coauthors, 2011: The community Noah land surface model with multiparameterization options (Noah-MP): 1. model description and evaluation with local-scale measurements. *Journal of Geophysical Research: Atmospheres*, **116** (D12), doi:10.1029/2010JD015139.
- O’Gorman, P. A., 2011: The effective static stability experienced by eddies in a moist atmosphere. *Journal of the Atmospheric Sciences*, **68** (1), 75 – 90, doi:10.1175/2010JAS3537.1.
- Queney, P., 1948: The problem of air flow over mountains: A summary of theoretical studies. *Bulletin of the American Meteorological Society*, **29** (1), 16 – 26, doi:10.1175/1520-0477-29.1.16.
- Ramesh, N., Q. Nicolas, and W. R. Boos, 2021: The globally coherent pattern of autumn monsoon precipitation. *Journal of Climate*, **34** (14), 5687 – 5705, doi:10.1175/JCLI-D-20-0740.1.
- Raymond, D., Ž. Fuchs, S. Gjorgjevska, and S. Sessions, 2015: Balanced dynamics and convection in the tropical troposphere. *Journal of Advances in Modeling Earth Systems*, **7** (3), 1093–1116, doi: <https://doi.org/10.1002/2015MS000467>.
- Roe, G. H., 2005: Orographic precipitation. *Annual Review of Earth and Planetary Sciences*, **33** (1), 645–671, doi:10.1146/annurev.earth.33.092203.122541.
- Satoh, M., B. Stevens, F. Judt, M. Khairoutdinov, S.-J. Lin, W. M. Putman, and P. Düben, 2019: Global cloud-resolving models. *Current Climate Change Reports*, **5** (3), 172–184.
- Skamarock, C., and Coauthors, 2019: A description of the Advanced Research WRF model version 4. Note NCAR/TN-556+STR, 145 pp.
- Smith, R., 1989: Hydrostatic airflow over mountains. *Advances in Geophysics*, **31**, 1–41.
- Smith, R. B., 1979: The influence of mountains on the atmosphere. *Advances in Geophysics*, **21**, 87–230, doi:10.1016/S0065-2687(08)60262-9.
- Smith, R. B., and I. Barstad, 2004: A linear theory of orographic precipitation. *Journal of the Atmospheric Sciences*, **61** (12), 1377 – 1391, doi:10.1175/1520-0469(2004)061<1377:ALTOOP>2.0.CO;2.
- Sobel, A. H., J. Nilsson, and L. M. Polvani, 2001: The weak temperature gradient approximation and balanced tropical moisture waves. *Journal of the Atmospheric Sciences*, **58** (23), 3650 – 3665, doi:10.1175/1520-0469(2001)058<3650:TWTGAA>2.0.CO;2.
- Thompson, G., P. R. Field, R. M. Rasmussen, and W. D. Hall, 2008: Explicit forecasts of winter precipitation using an improved bulk microphysics scheme. part II: Implementation of a new snow parameterization. *Monthly Weather Review*, **136** (12), 5095 – 5115, doi:10.1175/2008MWR2387.1.
- Wang, S., and A. H. Sobel, 2017: Factors controlling rain on small tropical islands: Diurnal cycle, large-scale wind speed, and topography. *Journal of the Atmospheric Sciences*, **74** (11), 3515–3532.
- Wing, A. A., and T. W. Cronin, 2016: Self-aggregation of convection in long channel geometry. *Quarterly Journal of the Royal Meteorological Society*, **142** (694), 1–15, doi:10.1002/qj.2628.
- Xie, S.-P., H. Xu, N. H. Saji, Y. Wang, and W. T. Liu, 2006: Role of narrow mountains in large-scale organization of asian monsoon convection. *Journal of Climate*, **19** (14), 3420 – 3429, doi:10.1175/JCLI3777.1.
- Yang, Z.-L., and Coauthors, 2011: The community Noah land surface model with multiparameterization options (Noah-MP): 2. evaluation over global river basins. *Journal of Geophysical Research: Atmospheres*, **116** (D12), doi:10.1029/2010JD015140.
- Yu, J.-Y., C. Chou, and J. D. Neelin, 1998: Estimating the gross moist stability of the tropical atmosphere. *Journal of the Atmospheric Sciences*, **55** (8), 1354 – 1372, doi:10.1175/1520-0469(1998)055<1354: ETGMSO>2.0.CO;2.
- Zhang, G., and R. B. Smith, 2018: Numerical study of physical processes controlling summer precipitation over the Western Ghats region. *Journal of Climate*, **31** (8), 3099 – 3115, doi:10.1175/JCLI-D-17-0002.1.